JEE Journal of Ecological Engineering

Journal of Ecological Engineering, 2026, 27(5), 57–73
https://doi.org/10.12911/22998993/215578
ISSN 2299–8993, License CC-BY 4.0

Received: 2025.12.02
Accepted: 2026.03.16
Published: 2026.04.01

Low-cost biosorbent derived from *Hermetia illucens* larval shells for competitive removal and adsorption mechanisms of lead(II), copper(II), and iron(III) ions

Wahyu Setiawan[1,2], Siska Nuri Fadilah[2], Euis Nurul Hidayah[3], Dyah Suci Perwitasari[4], Fakhili Gulo[2,5*]

[1] Department of Environmental Science, Universitas Pembangunan Nasional Veteran Jawa Timur, Surabaya 60294, East Java, Indonesia
[2] Department of Environmental Science, Postgraduate Program, Universitas Sriwijaya, Jl. Padang Selasa No. 524, Palembang 30139, South Sumatra, Indonesia
[3] Department of Environmental Engineering, Universitas Pembangunan Nasional Veteran Jawa Timur, Surabaya 60294, Indonesia
[4] Departement of Chemical Engineering, Faculty of Engineering, Universitas Pembangunan Nasional Veteran Jawa Timur, Surabaya 60294, East Java, Indonesia
[5] Study Program of Chemistry Education, Universitas Sriwijaya, Indralaya, Ogan Ilir 30662, South Sumatra, Indonesia
* Corresponding author's e-mail: fgulo@unsri.ac.id

ABSTRACT

Industrial wastewater containing a mixture of various heavy metals requires an adsorption technology capable of selective and efficient operation. This study examines *Hermetia illucens* larval shells (H. *illucens* LS) as unactivated biosorbents, characterizing their physicochemical properties and evaluating adsorption performance in a multi-metal batch system. XRD analysis indicates the dominance of $CaCO_3$ phases with contributions from chitin-based biopolymers; FTIR reveals changes in functional group vibrations associated with surface complexation and ion exchange mechanisms after metal interaction; BET analysis shows a specific surface area of 8.464 m^2/g with mesoporous characteristics, and SEM–EDX confirms pore narrowing and the presence of lead (Pb), iron (Fe), and copper (Cu) after adsorption. Selectivity tests involving seven metal ions demonstrate that Fe(III), Pb(II), and Cu(II) are preferentially adsorbed, forming the basis for mechanistic interpretation and the novelty of this study. The adsorption affinity follows the order Fe(III) > Pb(II) >> Cu(II), reflecting differences in charge density, coordination behavior, and competitive binding strength in multi-metal systems. Kinetic analysis indicates that adsorption follows a pseudo-first-order model which in this case is dominated by rapid initial interactions. Isotherm modeling shows that Fe(III), Pb(II), and Cu(II) are best described by the Freundlich model ($R^2 > 0.99$), confirming heterogeneous adsorption involving multilayer coverage. Thermodynamic parameters indicate that Fe(III) and Pb(II) adsorption is spontaneous and exothermic, whereas Cu(II) adsorption is less favorable due to weaker surface affinity. Overall, these findings demonstrate the intrinsic selectivity of *H. illucens* larval shells governed by surface chemistry rather than surface area, and support their potential as a cost-effective and sustainable biosorbent, with economic considerations discussed in this study, for multi-metal wastewater treatment.

Keywords: *Hermetia illucens*, black soldier fly, competitive adsorption, larval shells, multi-heavy metal ions.

INTRODUCTION

Heavy metal pollution is one of the most crucial global environmental problems due to its toxic, persistent, and non-biodegradable nature (Hidayah et al., 2025). Heavy metals such as lead (Pb), copper (Cu), and iron (Fe) are commonly found in industrial wastewater from industries such as electroplating, mining, metallurgy, and battery production (Elewa et al., 2023; Perwitasari et al., 2018; Wang et al., 2025). The accumulation of heavy metals in aquatic environments can have

serious impacts on aquatic biota and human health through bioaccumulation and biomagnification processes (Ali et al., 2019). Various conventional methods have been applied to remove heavy metals from wastewater, such as chemical precipitation (Han et al., 2024), coagulation-flocculation (Hussain et al., 2023), ion exchange (Rahmanian et al., 2017), biosorption (Imron et al., 2024), membrane filtration (Azmi et al., 2025), adsorption (Mei et al., 2025), and electrochemical processes (Tran et al., 2017). Although these methods have shown high effectiveness, several limitations remain, including high operational costs, large chemical requirements, secondary sludge formation, and decreased efficiency at low metal concentrations. These limitations have driven the development of more economical, environmentally friendly, and efficient processing technologies to address heavy metal problems.

One widely developed method is adsorption, considered a simple, effective, and flexible technique for removing heavy metal waste (Kothavale et al., 2023). In its development, this technology introduced the biosorption approach, namely the adsorption process by natural biomass or biological waste through complexation, ion exchange, or electrostatic interaction mechanisms (Imron et al., 2024). Biosorption efficiency is highly dependent on the characteristics of the biosorbent used, particularly its surface area, active functional groups, and ion exchange capacity (Fan et al., 2025). Biosorbent characteristics also depend on the type and composition of its primary material. The use of natural materials or biomass waste as biosorbents is currently attracting attention because it is economical and abundant, and also aligns with the principles of green chemistry and a circular economy (Sekaringgalih et al., 2025).

Biomass generally contains active groups such as –OH, –COOH, –NH_2, and –SH, which are capable of interacting with heavy metal ions (Yang et al., 2025). *Hermetia illucens* larval shell (*H. illucens* LS) biomass is an abundant but underutilized maggot cultivation waste product, offering significant potential as a natural biosorbent. Chemically, larval shells contain chitin (Bazan-Wozniak et al., 2025), protein, and calcium carbonate (Sharma and Thangadurai, 2025), which provide active sites for binding heavy metal ions through chemical and physical interactions. Unlike many other biomasses that require chemical activation or carbonization to increase adsorption capacity, *H. illucens* LS can be used directly after washing and drying. Their naturally porous structure (Bazan-Wozniak et al., 2025) and the presence of functional active groups allow for effective interaction with metal ions without the need for additional modification.

Research related to heavy metal adsorption using *H. illucens* has been widely reported in the literature. Several previous studies utilized *H. illucens* LS as a source of chitin-chitosan for Cd(II) and Ni(II) adsorption (Phasukarratchai et al., 2025; Złotko et al., 2021), *H. illucens* LS combined with activated carbon from biogas sludge for Cd(II) removal via capacitive deionization (Panja et al., 2025), zoo compost *H. illucens* as a Zn(II) ion biosorbent (Sverguzova et al., 2021), *H. illucens* larval feces for Cu(II) and Cd(II) adsorption (Zhang et al., 2020), and dead *H. illucens* biomass for Pb(II) adsorption (Zainudin et al., 2023). These studies generally focus on specific modification or activation processes and the adsorption evaluation of a single metal. In real wastewater conditions, heavy metal ions are typically present as mixtures of several metals, which can lead to competition between ions for active sites on the biosorbent surface and impact adsorption capacity and efficiency (Patel et al., 2024). However, studies using *H. illucens* LS biomass without chemical or thermal activation are still very limited. Therefore, this study examines the adsorption of multi-metals Pb(II), Cu(II), and Fe(III) using *H. illucens* LS through kinetics, isotherm, thermodynamics, and adsorption competition analysis, while complementing the study with an economic analysis to evaluate the potential of *H. illucens* LS as a low-cost green adsorbent that is feasible for large-scale water treatment applications. This study also contributes to sustainable development goals (SDGs) 12, 14, and 8 by supporting responsible consumption and production, preserving the quality of aquatic environments, and increasing the economic value of *H. illucens* agricultural waste for community and farmer-scale applications.

MATERIALS AND METHODS

Materials

H. illucens LS were obtained from local farmers in Pangandaran Regency, West Java, Indonesia. The reagents used in this study were of analytical grade with a purity >99%. Several heavy metals in the form of salts were used, including

$PbCl_2$, $CuCl_2 \cdot 2H_2O$, $FeCl_3 \cdot 4H_2O$, $CdCl_2 \cdot 2H_2O$, $CrCl_3$, $HgCl_2$, and $ZnCl_2$ (Merck, Germany), along with distilled water (OneMed, Indonesia).

Instrumentation

Functional groups were characterized using attenuated total reflectance Fourier-transform infrared (ATR-FTIR – Thermofisher Scientific Nicolet iS50, USA). Specific surface area was measured by the Brunauer-Emmett-Teller (BET) method (Quantachrome Quadrasorb EVO, USA). Crystalline phases were identified by X-ray diffraction (XRD, DX 2700, Haoyuan, China). Surface morphology and elemental mapping were obtained by scanning electron microscopy coupled with energy dispersive X-ray (SEM–EDX, JEOL JSM-6510LA, Japan). The centrifuged supernatant after adsorption was subjected to Atomic absorption spectrophotometer (AAS, PerkinElmer AAnalyst 800, USA).

Procedure

Preparation of biosorbent

The H. *illucens* LS biosorbent was initially washed with tap water to remove surface dirt, then rinsed with distilled water. The cleaned pellets were then dried in an oven at 105 °C (Memmert UN110, Germany) for 2 hours, the dried larval shells were then pulverized and sieved through mesh no. 40 to obtain pellets with a minimum size of 0.420 mm. The pellets were then reheated in the oven for 1 hour at 105 °C and put into a desiccator for 1 hour.

Preparation of heavy metal

Stock solutions were prepared from each heavy metal (Pb, Cu, Fe) at a concentration of 100 $mg \cdot L^{-1}$ and diluted to the desired concentration. The desired concentration was adjusted using dilution with a certain ratio.

Adsorption selectivity test

A mixture solution of seven heavy metal ions (Pb(II), Cu(II), Fe(III), Zn(II), Ni(II), Cd(II), and Cr(III)) was prepared and combined with an initial concentration of 100 $mg \cdot L^{-1}$ each. The mixture was then treated with a biosorbent at a ratio of 10 $g \cdot L^{-1}$ and a shaker speed of 160 rpm for 1440 min. After adsorption, the biosorbent was centrifuged, and AAS analyzed the residual concentrations of each ion to evaluate the biosorbent's relative adsorption capacity and selectivity in a competitive multi-ion system. All adsorption experiments were conducted without pH adjustment, and the initial solution pH remained close to neutral (≈7) due to the use of distilled water.

Adsorption kinetics, isotherms, and thermodynamic studies

The adsorption kinetics were studied by diluting heavy metal stock solutions into 100 ml Erlenmeyer flasks with the following concentrations: 90 $mg \cdot L^{-1}$ for Pb(II), 85 $mg \cdot L^{-1}$ for Cu(II), and 75 $mg \cdot L^{-1}$ for Fe(III). A total of 1 g of biosorbent was added to a 250 mL Erlenmeyer flask (Pyrex, Germany) containing 100 mL of heavy metal solution. The mixture was shaken in a Shaker incubator (B-One SIC 50L, China) at 160 rpm for 30, 60, 180, 360, 720, and 1440 minutes, then centrifuged at 12,000 rpm for 5 minutes. The adsorption isotherms and thermodynamic properties were studied at 308, 318, and 328 K. The concentration variations were 2, 4, 6, 8, 10, and 12 $mg \cdot L^{-1}$ prepared using the same dilution method, shaker speed, and biosorbent weight. Contact was performed at equilibrium time, then the mixture was centrifuged. The centrifugation results yielded a pellet (biosorbent after adsorption), which will then be characterized, and the supernatant was subjected to AAS with three replications. Adsorption removal efficiency (%) for heavy metals and adsorption capacity were calculated by using Equation 1 and 2.

$$\text{Adsorption removal efficiency (\%)} = = \frac{C_0 - C_{eq}}{C_0} \times 100 \quad (1)$$

$$\text{Adsorption capacity (mg / g)} = = \frac{C_0 - C_{eq} \times V}{m} \quad (2)$$

where: C_0 – initial concentration ($mg \cdot L^{-1}$), C_{eq} – final concentration ($mg \cdot L^{-1}$), m – mass of biosorbent (g), V – volume of solution (L).

RESULTS AND DISCUSSION

Characteristic biosorbent

Crystallinity

The XRD pattern of *H. illucens* LS is shown in Figure 1, displaying a series of sharp and well-defined peaks, confirming its crystalline nature. The

diffraction peaks at 2θ = 9.2°, 19.3°, 23.1°, and 26.3° are characteristic of the crystalline structure of α-chitin (Zewude et al., 2022). The main diffraction reflections appear at around 29.4°, 36.0°, 39.5°, 43.2°, 47.6°, and 48.5°, which correspond to the (104), (110), (113), (202), (018), and (116) planes of calcite ($CaCO_3$) according to JCPDS card No. 05-0586. The dominance of the (104) reflection at 29.4° is characteristic of biogenic calcite, indicating the regular crystal orientation common in naturally mineralized calcium carbonate. The relatively narrow and intense diffraction peak indicates a high degree of crystallinity, reflecting the strong and compact structure typical of biomineralized $CaCO_3$ frameworks.

The absence of additional reflections indicates that the *H. illucens* LS is composed almost entirely of calcite (Ouyang et al., 2024), which is the most stable polymorph of $CaCO_3$. This crystalline stability implies that the $CaCO_3$ phase in the *H. illucens* LS is structurally persistent and resistant to chemical transformation under normal environmental conditions. The regular calcite lattice also contributes to its mechanical rigidity and surface stability, both of which are favorable characteristics for its potential application as a low-cost and structurally stable sorbent material.

Functional groups

The ATR-FTIR spectra of *H. illucens* LS before and after adsorption (Figure 2) show clear spectral changes, confirming the active participation of surface functional groups in heavy metal binding. The broad absorption band at 3296 cm^{-1}, originating from the stretching vibrations of –OH and –NH (functional groups of chitin), shifts to 3259 cm^{-1}, indicating the involvement of hydroxyl and amine groups in coordination or hydrogen bonding with metal ions (Phasuphan et al., 2019; Zhao et al., 2021). The appearance of additional peaks at 2164, 2027, and 1965 cm^{-1}, evolving from the initial band at 2162 cm^{-1}, indicates the formation of new interactions between carbonyl or amide groups and metal centers through M–C=O or M–N bonds. (Table 1).

The shift of the $–COO^-$/amide II band from 1393 cm^{-1} to a broader region, 1542–1614 cm^{-1}, further supports the complexation of carboxylic and amide groups with metal ions (Zewude et al., 2022). The slight shift of the C–O/C–O–C band from 1018 to 1014 cm^{-1} reflects the interaction between polysaccharide or chitin components and surface metal species (Zhao et al., 2021). Furthermore, the emergence of new absorption bands at 674, 599, and 539 cm^{-1} indicates metal–oxygen (M–O) vibrations, providing clear evidence of chemical bonding between the metal and oxygenated groups (Muharja et al., 2023; Zhang et al., 2019).

Specific surface area

The BET method revealed that the specific surface area of the *H. illucens* LS was 8.099 $m^2 \cdot g^{-1}$, with a total volume and an average pore

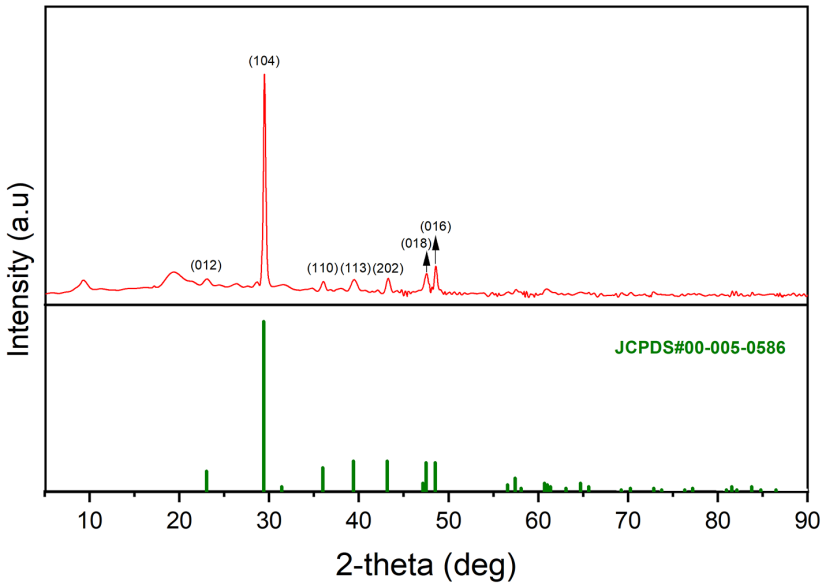

Figure 1. XRD pattern of *H. illucens* LS

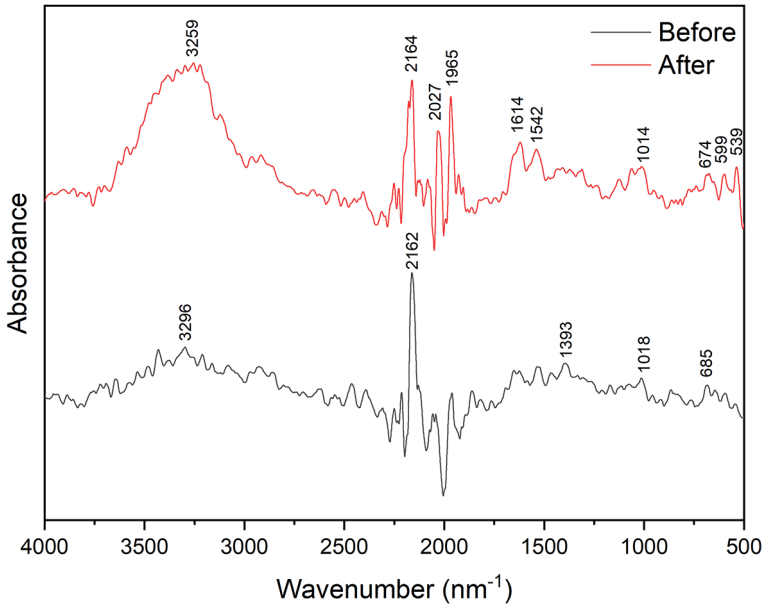

Figure 2. FTIR spectrum of *H. illucens* LS before and after adsorption

Table 1. FTIR peak positions before and after adsorption

No	Before (cm^{-1})	After (cm^{-1})	Functional groups	Interpretation
1	3296	3259	–OH, –NH, H-bond	Involvement of hydroxyl/amine groups in coordination or hydrogen bonding with metal ions.
2	2162	2164, 2027, 1965	C≡O / C≡N	The formation of new complexes or changes in the chemical environment of carbonyl/amide groups due to metal coordination.
3	1393	1542–1614	$–COO^-$, amide II, –CH	Involvement of carboxylic/amide groups in the formation of coordination bonds with metal cations.
4	1018	1014	C–O, C–O–C	Interaction between C–O groups in polysaccharides/ chitin and metal ions.
5	(not clearly visible)	674, 599, 539	(M–O)	Confirmation of M–O complexation or strong physicochemical adsorption.
6	685	—	($CaCO_3$)	Changes in the surface inorganic components (native Ca^{2+} is replaced/affected by M^{2+}/M^{3+}) that support the ion exchange mechanism.

diameter of 0.010 $cm^3 \cdot g^{-1}$ and 16.322 nm, respectively. *H. illucens* LS can be classified as a mesoporous material because its pore diameter ranges from 2–50 nm according to the International Union of Pure and Applied Chemistry (IUPAC) classification (Rouquerol et al., 1994). The N_2 adsorption-desorption isotherm (Figure 3) shows a type III profile, indicating weak N_2–surface interactions and multilayer adsorption at higher pressures (Sun et al., 2022). Despite its relatively low BET surface area, H. *illucens* LS exhibits effective adsorption performance towards heavy metal ions. This is because BET analysis reflects the physical adsorption of N_2 rather than the availability of chemically active sites for ionic species. In this study, metal adsorption was controlled by surface complexation mechanisms with functional groups and ion exchange. The mesoporous structure primarily facilitates solution diffusion and accessibility to reactive sites rather than directly determining adsorption capacity (Motitswe et al., 2022). Comparison with other $CaCO_3$ materials (Table 2) shows that the surface area of *H. illucens* LS is comparable to or slightly higher than that of similar biomineral matrices, further supporting that adsorption efficiency is controlled by surface chemistry rather than physical surface area alone.

Morphology

The SEM micrographs of the *H. illucens* LS before and after adsorption (Table 3) show an irregular microstructure composed of compact

Table 2. Comparison of the surface area of the present biosorbent with previously reported

Materials	Surface area (m^2/g)	Pore volume (cm^3/g)	Pore diameter (nm)	References
Shrimp shells	5.027	0.0310	38.160	(Misran et al., 2025)
Giant mud crab	26.400	0.1150	23.100	(Mohd Faizal et al., 2024)
Freshwater mussel shells	1.450	0.0002	-	(Van et al., 2019)
Biochar-NH_2 of watermelon peels	12.260	0.0120	5.940	(El-Nemr et al., 2024)
Oyster shell	2.160	0.0067	-	(Hussain et al., 2025)
Chicken eggshell powder	0.692	0.0010	*3.597*	(Praipipat et al., 2023)
H. illucens LS	8.464	0.0101	2.393	*This study*

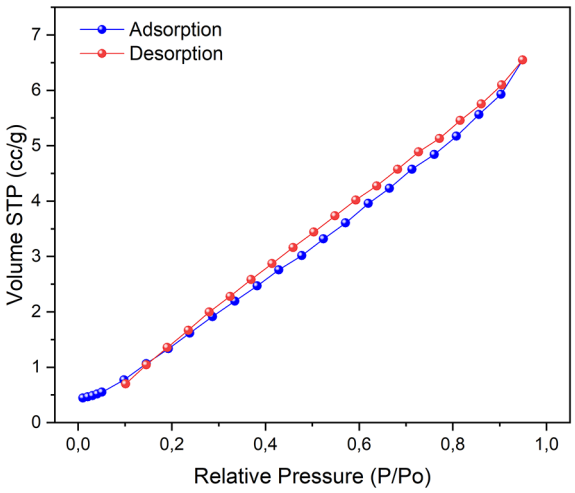

Figure 3. N_2 adsorption-desorption isotherm of *H. illucens* LS

plate-like particles and fibrous fragments, characteristic of biogenic mineral–organic composites (Van et al., 2019). The surface exhibits a heterogeneous texture with both dense and porous regions, indicating a well-integrated matrix between mineralized calcium carbonate domains and carbonaceous organic matter derived from the larval exoskeleton. Such structural complexity provides a high surface heterogeneity that can favor metal ion interaction through various active sites. After adsorption, the surface morphology appears slightly rougher and more compact, suggesting the partial occupation of surface pores and the attachment of heavy metal ions on the shell matrix, in line with the EDX results.

Complementary EDX analysis (Figure 4) confirms the composite nature of the material. The pristine *H. illucens* LS consists mainly of carbon, oxygen, and calcium, accompanied by minor elements such as Mg, P, S, and K. This composition aligns with a $CaCO_3$–protein/chitin hybrid matrix, in line with XRD result. After exposure to the multi-metal solution, new peaks corresponding to Fe, Cu, and Pb emerge, verifying the successful immobilization of heavy metal ions on the surface. The decrease in Ca alongside the persistence of a high carbon fraction suggests that adsorption predominantly occurs via surface complexation and coordination with functional groups rather than through extensive ion exchange with calcium. In addition, the increased nitrogen content after adsorption reflects the contribution of organic moieties, likely amine or amide groups, in metal binding.

The elemental mapping images (Figure 5) show a uniform and intense Ca distribution across the shell surface, confirming the homogeneity of the mineral matrix. Meanwhile, Fe and Pb signals are evenly dispersed throughout the surface rather than localized in isolated regions, evidencing that the adsorbed metals are well distributed across the biosorbent surface. This uniform dispersion supports the hypothesis that metal uptake occurs through surface complexation or electrostatic interaction at multiple active sites rather than through bulk precipitation.

The three-dimensional reconstruction of the *H. illucens* LS (Figure 6) reveals a highly porous and irregular surface with interconnected voids that form a continuous open framework, obtained using a previously reported method (Setiawan et al., 2026b). Quantitative volumetric analysis (Table 4) shows that the porosity before adsorption was 70.38%. After adsorption of mixed heavy metals (Pb, Cu, and Fe), the porosity drops to 64.65%, indicating a measurable reduction of approximately 8%. This decline demonstrates that metal ions were successfully immobilized on the biosorbent surface, partially filling or coating the internal pores and thereby reducing the overall void fraction. The narrowing of pore channels suggests that adsorption

Table 3. SEM images of the *H. illucens* LS biosorbent before and after heavy-metal adsorption at various magnifications

Mag	Before adsorption	After adsorption
1000x	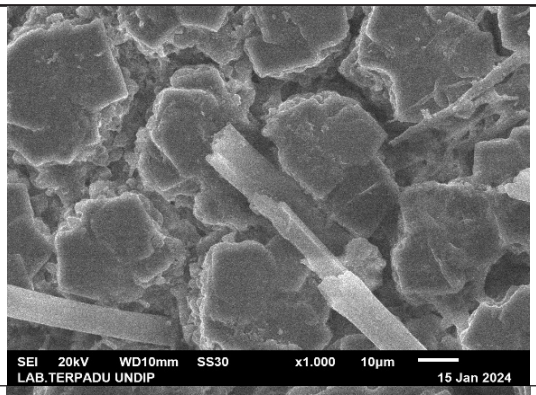	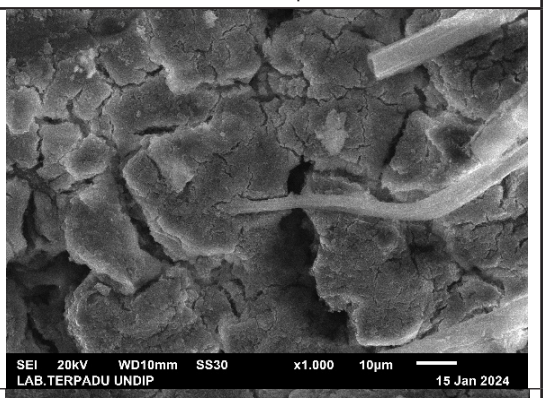
2000x	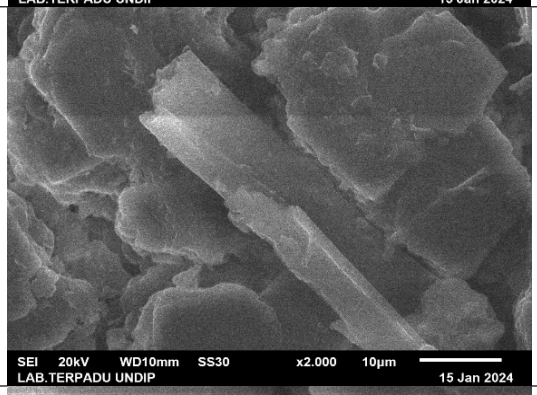	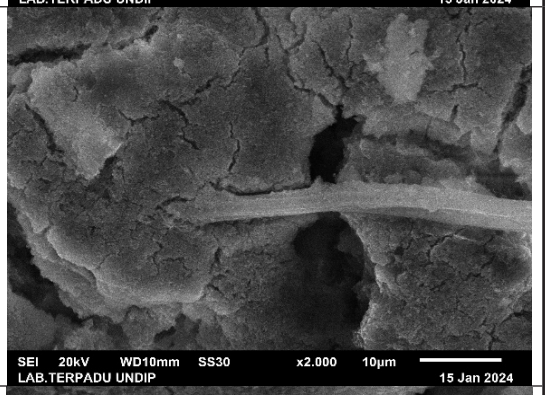
5000x	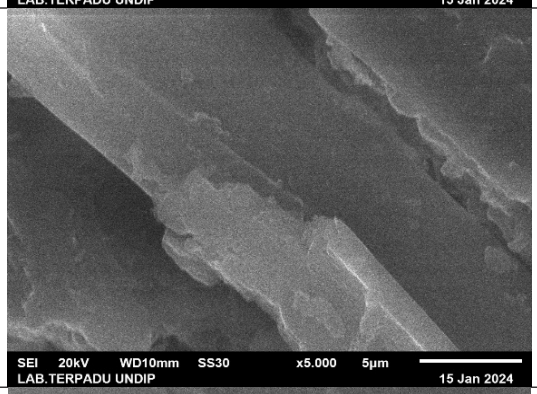	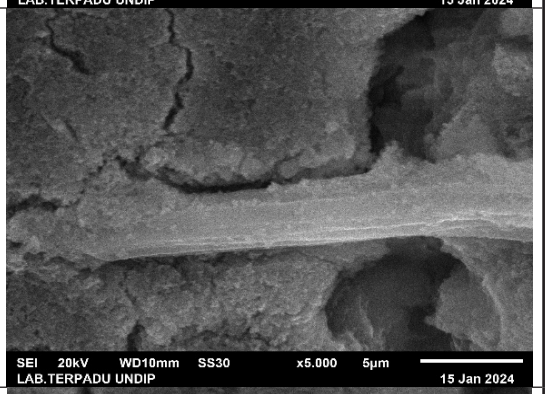
10000x	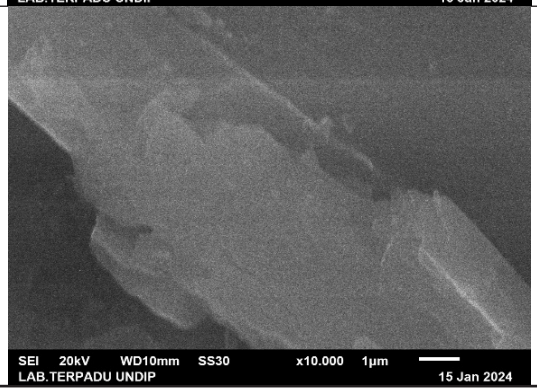	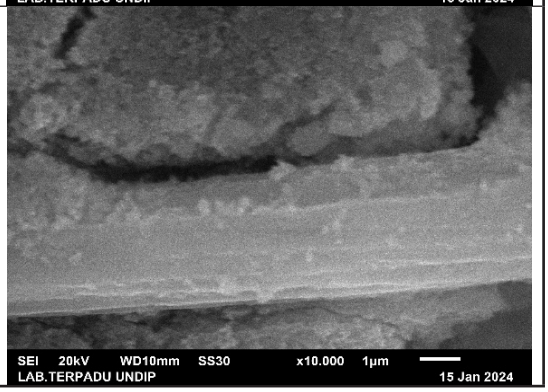

primarily occurred through surface deposition and interaction at accessible sites, rather than through deep structural changes. Despite the decrease, the *H. illucens* LS maintained a well-connected porous network, implying that its structural framework remained intact and capable of facilitating ion diffusion and multi-metal adsorption processes efficiently.

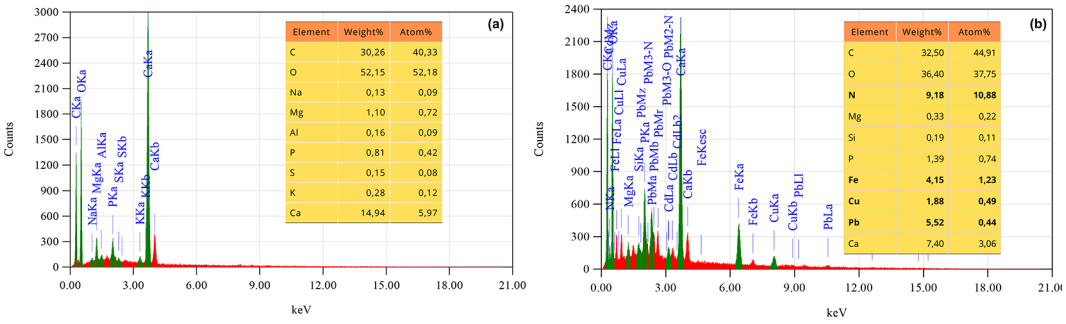

Figure 4. EDX spectra of the biosorbent (a) before and (b) after heavy metals adsorption

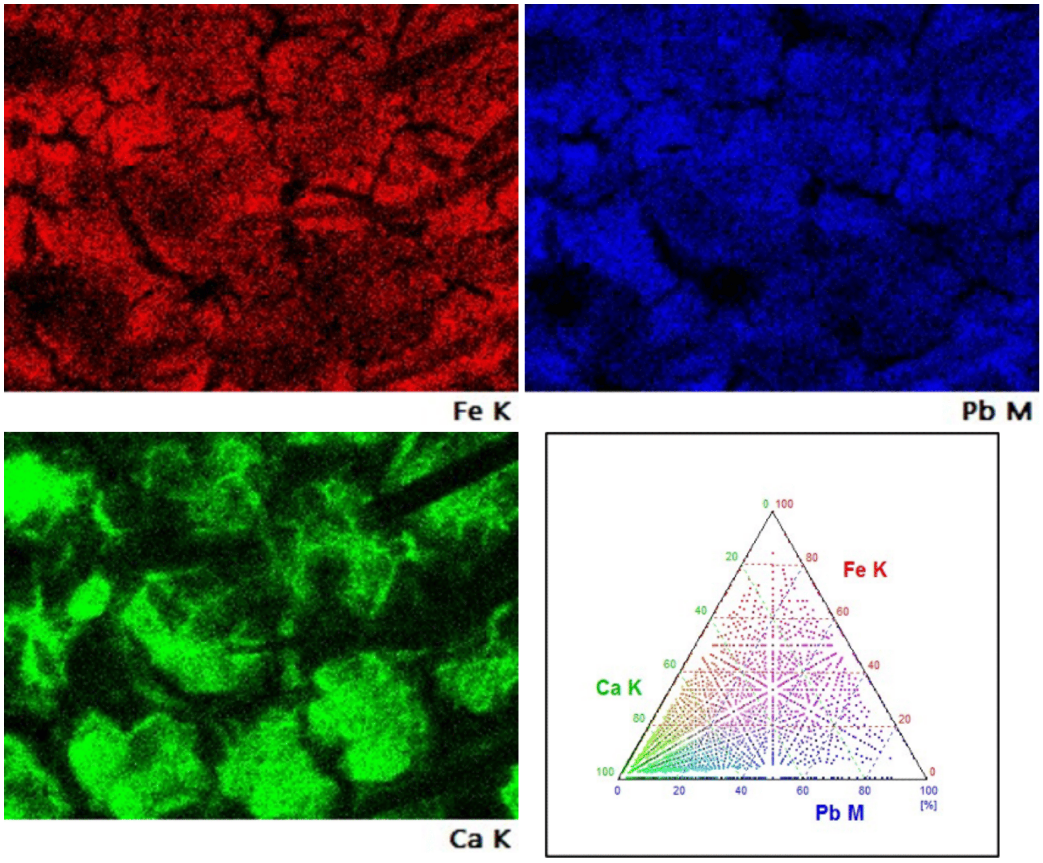

Figure 5. Dispersed heavy-metal species on the biosorbent after adsorption

Preliminary selectivity test of the biosorbent

This analysis aims to determine the selective adsorption behavior of the biosorbent and identify which metal ion is preferentially captured under the tested conditions. The results are presented in Figure 7. Selectivity tests on multi-metal systems show that Pb(II), Cu(II), and Fe(III) are the most dominant ions adsorbed, reflecting the ability to form more stable coordinative interactions with active groups in the protein-chitin-melanin matrix. The stability of the complex allows the metal to dominate high-energy sites and maintain its attachment despite competition with other ions. In contrast, Cd(II), Cr(III), Hg(II), and Zn(II) show lower adsorption capacities because the interactions formed tend to be weak, hampered by a larger hydration radius, lower effective charge density, or a tendency to form less stable complexes, which are easily displaced during competition. This pattern confirms that the natural biopolymer structure of the *H. illucens* LS exhibits an intrinsic selective response, enabling it to prioritize high-affinity ions under complex heavy-metal mixture conditions.

Table 4. 3D SEM–based porosity parameters before and after adsorption

Material	Parameter	Value	Unit
Before adsorption	Volume total	1.0×10^{10}	m^3
	Solid volume (V solid)	4.0×10^{9}	m^3
	Pore volume (V pori)	9.0×10^{9}	m^3
	Porosity	70.38	%
After adsorption	Volume total	1.0×10^{10}	m^3
	Solid volume (V solid)	4.0×10^{9}	m^3
	Pore volume (V pori)	8.0×10^{9}	m^3
	Porosity	64.65	%

Competitive adsorption mechanisms of heavy metals

The removal efficiency of three types of heavy metal ions (Pb, Fe, and Cu) by *H. illucens* LS biosorbent at various contact times is shown in Figure 8. The biosorbent exhibits very high selectivity for Fe, with removal efficiencies approaching 100% over all contact times. This indicates that the active sites on the biosorbent have a strong affinity for Fe, resulting in a very rapid adsorption process that is largely unaffected by contact time. For Pb, the adsorption efficiency was also high, with a relatively stable increase over time, indicating that Pb can be effectively bound by the biosorbent. Conversely, Cu exhibited very low adsorption efficiency, indicating that the biosorbent has very limited affinity for Cu. However, Cu ions began to be significantly adsorbed only after most of the active sites were dominated by Fe and Pb, when the adsorption process of both ions had approached saturation.

Adsorption of heavy metal ions depends on the physical and chemical properties of the metal ions, such as the hydrolysis constant and the hydrated ion radius. The lower the hydrolysis constant of a metal ion, the more readily it is adsorbed (An et al., 2024). The hydrolysis constants of the three ions are respectively Fe(III)<Pb(II)<Cu(II), Fe(III) is significantly lower than Pb(II) and Cu(II). For homogeneous metal cations, the smaller the hydration radius, the easier it is to diffuse through the boundary layer to the surface of the adsorbent. The hydration radius of Fe(III) is 0.268 nm (Zhibo et al., 2018), Pb(II) is 0.401 nm (Radovanovic et al., 2023), and Cu(II) is 0.419 nm (Bowron et al., 2013). The hydration radius value indicates resistance to increasing mass, the smaller the value, the more likely ion exchange reactions occur, this explains the higher adsorption of Fe(III) and Pb(II).

The adsorption behavior of Pb(II), Cu(II), and Fe(III) on *H. illucens* LS without activation is controlled by a synergy of several mechanisms originating from the $CaCO_3$–chitin–protein–melanin matrix (Figure 9). As supported by the FTIR and EDX results discussed previously, the metal immobilization process does not occur through a single mechanism, but rather through a combination of ion exchange, surface complexation, outer-sphere interactions, and the contribution of physical adsorption in the mesopores. Ion exchange occurs partially through the substitution of Ca^{2+} and Mg^{2+} cations by heavy metal ions, especially Pb(II) and Fe(III), which have higher binding affinities, as evidenced by the significant decrease in Ca and Mg contents after adsorption (Złotko et al., 2021). Meanwhile, surface complexation plays

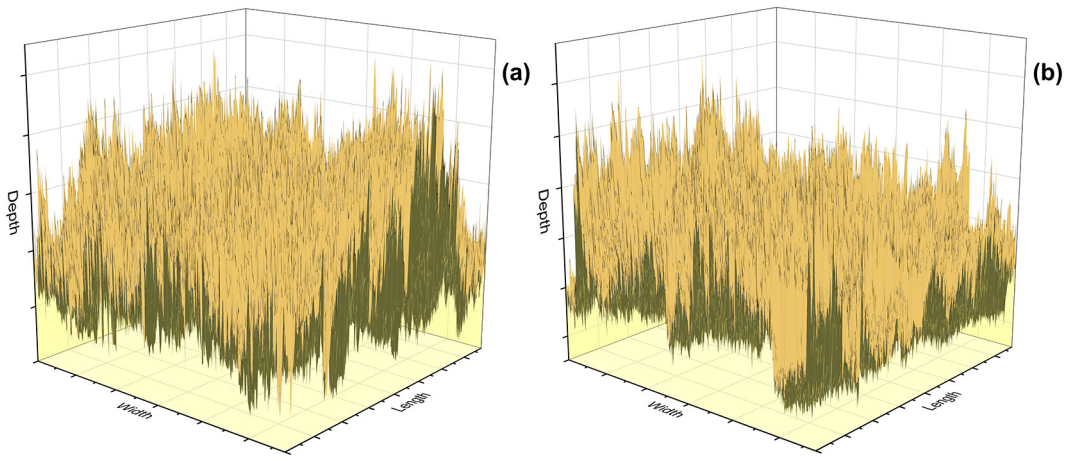

Figure 6. 3D representation of porous structure of *H. illucens* LS biosorbent before (a) and after (b) adsorption

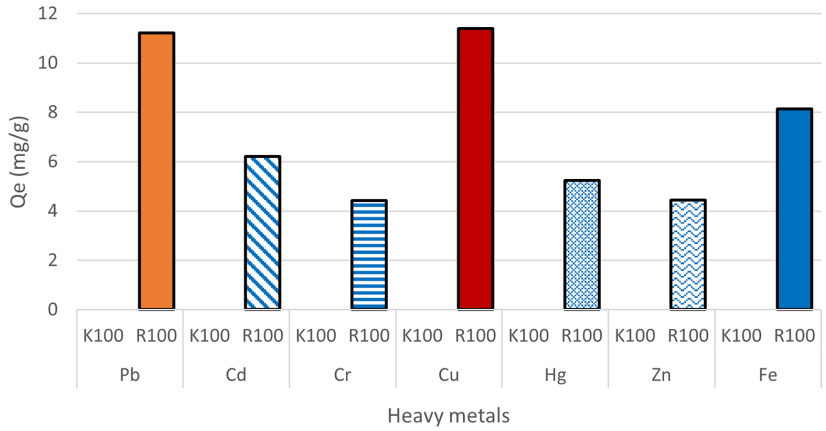

Figure 7. Adsorption selectivity test

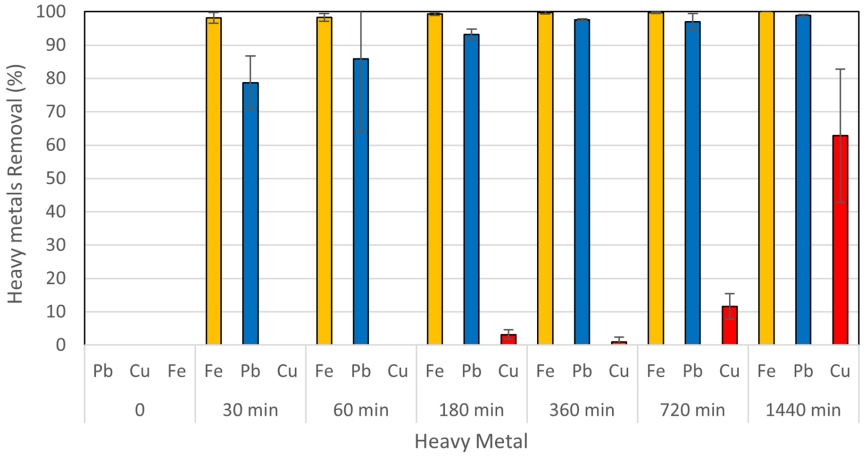

Figure 8. Removal of Pb-Cu-Fe during adsorption tests by *H. illucens* LS biosorbent

a crucial role in determining selectivity, where the –OH, –C=O, and –NH_2 functional groups of chitin, protein, and melanin act as ligand donor sites, as evidenced by FTIR results after adsorption, as well as the order of preferential adsorption results of Fe(III) > Pb(II) > Cu(II). Fe(III) with the highest charge density can act as a hard Lewis acid, thus exhibiting a strong affinity for hard base donor groups such as –OH and $–COO^-$, leading to rapid adsorption (Alfarra et al., 2004). Pb(II) and Cu(II), which are classified as borderline acids, exhibit weaker interactions with these functional groups.

In multi-metallic systems, competitive adsorption further enhances this selectivity, as Fe(III) and Pb(II) preferentially occupy high-affinity sites, thus limiting the availability of binding sites for Cu(II) and resulting in delayed and lower adsorption. At near-neutral pH conditions without special adjustment, the metal immobilization process likely involves a combination of surface adsorption and local hydroxylation interactions at the biosorbent interface, without the formation of macroscopic precipitation in solution that cannot be completely separated, but still contributes to the binding of metals to the *H. illucens* LS matrix.

Kinetic study

In general, the adsorption process proceeds through three main stages: (1) film diffusion on the adsorbent surface, (2) intra-particle diffusion, and (3) adsorption on active sites within the pores. The duration required for each stage contributes to the overall rate of the adsorption process (Li et al., 2019). As shown in Figure 10, the kinetic characteristics of Fe(III) and Pb(II) adsorption by *H. illucens* LS were analyzed and compared, while kinetic data for Cu(II) could not be obtained because its adsorption process had not reached equilibrium within the studied time span (see Figure 8). In the

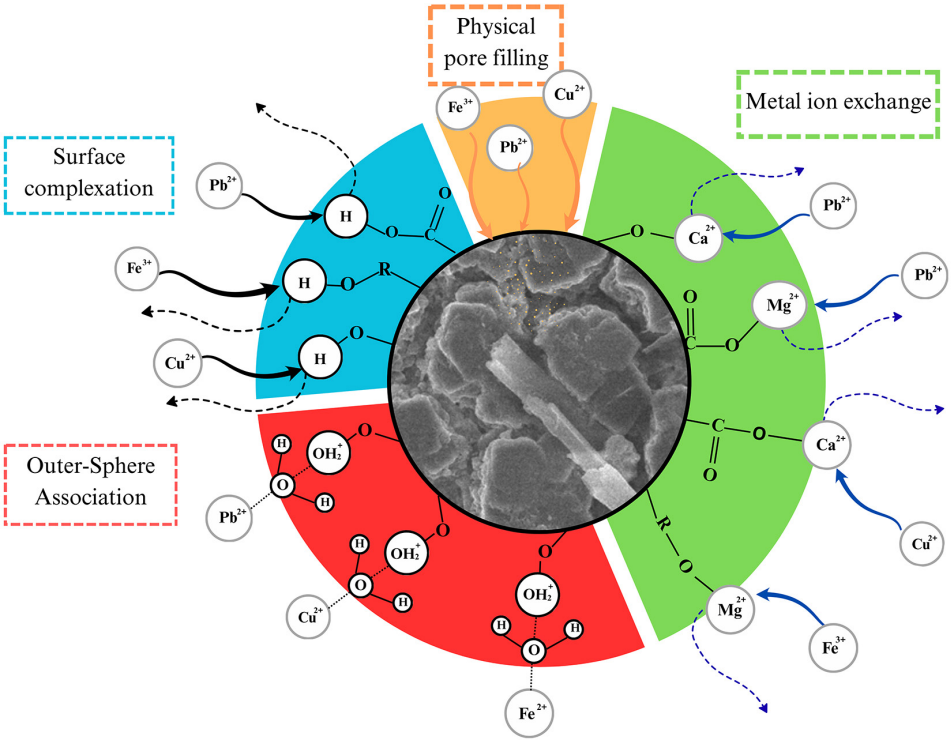

Figure 9. Multi-metal adsorption mechanism

initial stage of adsorption, the adsorption capacities of both ions increased sharply. For Fe(III), the adsorption capacity reached saturation early on and thus did not show a significant increase with increasing contact time, indicating rapid adsorption. In contrast, Pb(II) adsorption showed a gradual increase in capacity and reached equilibrium after approximately 6 hours. This pattern confirms that Pb(II) adsorption proceeds through two stages: a rapid adsorption stage followed by a slow adsorption stage.

Pseudo-first-order (PFO) and pseudo-second-order (PSO) adsorption kinetic models were used to model the adsorption of Fe(III), Pb(II), and Cu(II) by *H. illucens* LS, with the aim of evaluating the rate-controlling steps of adsorption. The obtained kinetic parameters are presented in Table 5. The modeling results show that Fe(III) adsorption follows the PFO model with an R^2 value of 1 and low sum of squared errors (SSE) and root mean square error (RMSE) values. The calculated Qe value (Qe_1) is also identical to the experimental value (Qexp), indicating that the Fe(III) adsorption rate is mainly controlled by the rapid initial stages, such as external diffusion and active surface accessibility. In contrast, Pb(II) adsorption showed almost the same fit to both models, so the kinetic models were not sensitive enough to distinguish the adsorption mechanisms in this system. This condition is likely caused by competition between metal ions that affect surface interactions. The rate constant K_1 value in the PFO model indicates that Fe(III) adsorption occurs faster than Pb(II), and a similar trend is also shown by the K_2 value in the PSO model. This finding is consistent with the adsorption pattern in Figure 8 and is in line with the factors previously explained.

Although the adsorption kinetics follow a pseudo-first-order model, this does not imply purely physical adsorption. Kinetic models describe the rate-limiting step, which in this case is dominated by rapid initial interactions such as electrostatic attraction and external diffusion. FTIR analysis indicates that, upon reaching equilibrium, heavy metal ions form coordinative bonds with surface functional groups, confirming the involvement of chemisorption. Thermodynamic analysis further supports the spontaneous nature of the process, with negative Gibbs free energy values reflecting the combined contributions of physical adsorption, ion exchange, and surface complexation. Therefore, the adsorption of Fe(III), Pb(II), and Cu(II) onto *H. illucens* LS proceeds via a hybrid, multi-step mechanism rather than a single adsorption pathway.

Table 5. Kinetic parameters for the adsorption

Heavy metals	Q_{exp} (mg/g)	Pesudo first-order					Pseudo second-order				
		Qe_1 (mg/g)	K_1 (min^{-1})	R^2	SSE	RSME (mg/g)	Qe_2 (mg/g)	K_2 ($g.mg^{-1}min^{-1}$)	R^2	SSE	RSME (mg/g)
Fe	7.63	7.63	0.131	1	0.020	0.054	5.97	5.53693	0.88664	15.865	1.505
Pb	9.14	9.09	0.052	0.99989	0.837	0.345	9.19	0.01378	0.99998	0.099	0.119
Cu	-	-	-	-	38.034	2.330	-	-	-	38.034	2.330

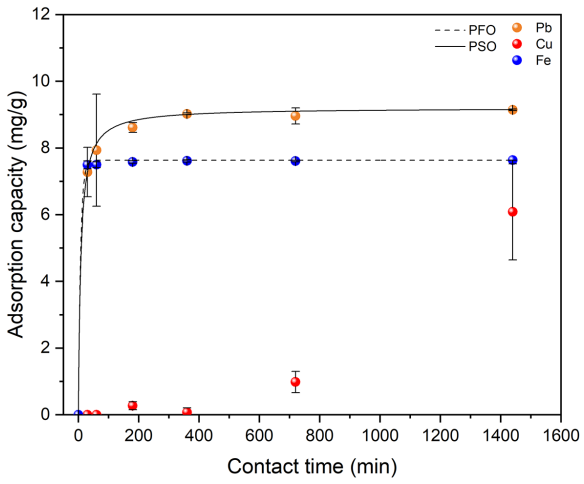

Figure 10. Effect of contact time on the adsorption different heavy metals

Isotherm and thermodynamic study

Isothermal models such as the Freundlich and Langmuir models were applied to simulate data from experiments, and the correlation coefficient (R^2) (Table 6). Although relatively high R^2 values were obtained for the Langmuir model, the Freundlich model provided a consistently better fit for Fe(III), Cu(II), and Pb(II), indicating adsorption on energetically heterogeneous surfaces rather than ideal monolayer coverage (Vigdorowitsch et al., 2021). The suitability of the Freundlich model is further supported by the Freundlich intensity parameter (n), which reflects adsorption favorability and surface heterogeneity. The obtained n values (>1) indicate favorable adsorption and confirm the presence of multiple binding sites with different affinities. This behavior is consistent with the complex biopolymeric composition of *H. illucens* LS, consisting of chitin, protein, and melanin, which provides a wide distribution of electron-donor functional groups. The relatively good fit of the Langmuir model suggests that, at low to intermediate metal concentrations, adsorption may initially proceed via site-specific interactions approaching localized monolayer coverage. However, as metal concentration increases, additional adsorption occurs on lower-energy sites, resulting in a multilayer or non-uniform adsorption process better described by the Freundlich model. This combined isotherm behavior implies a mixed adsorption mechanism, where surface complexation dominates at high-affinity sites, followed by secondary interactions on heterogeneous domains. The maximum adsorption capacities presented in Table 7 further confirm that, even without chemical or thermal activation, the shell of *H. illucens* larvae functions as a naturally optimized biosorption matrix. The tightly bound network of chitin, protein, and melanin forms a stable and functional structure that facilitates effective metal binding, distinguishing it from conventional chitin materials that require extensive purification or activation to achieve comparable performance (Khayrova et al., 2021; Pedrazzani et al., 2024).

The thermodynamic parameters obtained from the adsorption process are presented in Table 8. Thermodynamic parameters provide further insight into the nature of the bond energies formed (Setiawan et al., 2026). The negative ΔH values for all three metals indicate that the adsorption process is exothermic, resulting in the release of energy for metal-surface interactions, consistent with the formation of stable surface complexes. The ΔG values reveal essential differences between the metals: Fe(III) and Pb(II) exhibit negative ΔG at all temperatures, indicating that their adsorption is spontaneous and thermodynamically favorable. Conversely, Cu(II) shows a positive ΔG, suggesting that its adsorption is non-spontaneous and energetically less favorable, requiring specific mechanisms, such as local interactions with functional groups or external energy assistance, to proceed. The negative ΔS values for all metals indicate a decrease in the entropy of the system, which can be interpreted as the formation of a more ordered complex structure on the surface, in line with the metal-ligand coordination

Table 6. Isotherm parameters of Langmuir and Freundlich model for the adsorption

Heavy metals	T (K)	Langmuir constants			Freundlich constants		
		Q_{max} (mg/g)	K_L	R^2	n	K_f	R^2
Fe	308	15.7	0.0156	0.91759	1.0088	0.1877	0.99951
	318	16.2	0.0160	0.88398	1.0339	0.1848	0.98823
	328	17.03	0.0168	0.84417	1.1265	0.1597	0.99851
Cu	308	15.16	0.01513	0.93562	0.8931	0.2324	0.99708
	318	15.41	0.01536	0.92871	0.9146	0.2264	0.99681
	328	15.55	0.01547	0.92263	0.9855	0.1948	0.99884
Pb	308	9.42	0.00836	0.77447	1.1591	0.0508	0.7924
	318	9.62	0.00779	0.53033	1.3330	0.0329	0.5688
	328	9.80	0.00881	0.72864	2.1459	0.0056	0.9495

Table 7. Comparison of adsorption capacities in multi-ion heavy metal systems

No	Adsorbents	Adsorption capacity (mg/g)			References
		Fe(III)	Pb(II)	Cu(II)	
1.	Fly ash	0.19	0.01	0.27	(Hamed and Abdallah, 2024)
2.	Norway spruce wood residue (NSWR)	N/A	6.30	7.90	(Al-Labadi et al., 2025)
3	AC waste rubber tire	N/A	9.68	12.43	(Cherono et al., 2021)
4.	Ceramic sorbent	N/A	2.26	2.29	(Zhu et al., 2021)
5	Treated shrimp shell waste (TSSW)	N/A	15.32	22.67	(Boddu et al., 2022)
6	Activated orange peels (AOP)	9.11	N/A	N/A	(Adebayo et al., 2016)
7	Activated carbons derived from recyclable long-root *Eichhornia crassipes*	N/A	1.34	1.07	(Cao et al., 2019)
8	Activated carbon residue from biomass gasification	21.00	N/A	23.00	(Runtti et al., 2014)
9	H. *illucens* LS	17.03	9.80	15.55	This study

Table 8. The thermodynamic parameters for heavy metals adsorption

Adsorption processes	ΔH (J/mol)	ΔS (J/mol·K)	R^2	ΔG (J/mol)		
				308	318	328
Fe	-5455.55	-3.133	0.99251	-4490.49	-4459.16	-4427.83
Cu	-2209.27	-14.265	0.91618	2184.42	2327.07	2469.72
Pb	-6626.55	-6.680	0.32384	-4568.95	-4435.34	-4435.34

process that binds hydrated water molecules and rearranges organic functional groups.

Cost analysis

The cost of an adsorption system is a critical factor determining the feasibility of the process, especially in remote areas and low-income countries. Cost-effectiveness is highly dependent on the cost of the adsorbent. Several previous reports have identified the cost of adsorbent synthesis based on its origin and the number of modification steps required (Muharja et al., 2022). One strategy to minimize costs is the use of adsorbents from with little or no preparation steps (Dehghani et al., 2023). This approach specifically reduces potential environmental and economic problems, in line with this study's use of waste with process minimization. The estimated cost to produce 1 kg of adsorbent in this study was calculated by considering the amount of material and energy consumption, as shown in Table 9.

A material can be categorized as low cost if its preparation cost is less than 1 US dollar per kilogram (Kumar et al., 2019), therefore the adsorbent in this study is low-cost. The comparison

Table 9. Cost estimation for 1 kg biosorbent production

Component	Quantity	Cost (IDR)	Cost ($USD)
H. *illucens* LS waste	1 g	-	-
Distillate water	1 L	5000	0.300
Energy for drying	1.8 kWh	2400	0.140
Total		7400	0.440
Other overhead costs	10% of total cost	740	0.044
Total cost		8140	0.484

Table 10. Cost comparison between biosorbent product in this study with other adsorbent

Adsorbent	Target pollutant	Adsorption capacity	Cost ($/kg)	References
High chitosan-polyvinyl alcohol (CSPVA)	Cu and Fe	230.91 and 71.48 mg/g	1,435	(Patel et al., 2025)
Activated carbon from waste cherry kernels	Pb^{2+} and Cd^{2+}	N/A	41.92	(Vukelic et al., 2018)
Magnetic *Juglans Regia* shell biochar	Cu^{2+}	16.83 mg/g	1.89	(Isaac et al., 2023)
Modified canola straw biochars	As(V)	848 µg/g	5.14	(Norberto et al., 2023)
Rice straw-based biochar	Sr(II)	687.8 µmol/g	0.56±0.02	(Younis et al., 2020)
H. *Illucens* LS	Pb(II), Cu(II), and Fe(III)	9.80, 15.55, and 17.03 mg/g	0.484	*This study*

of adsorbent costs in Table 10 shows that engineered adsorbents such as CSPVA offer high capacity, but are very expensive and therefore less suitable for large-scale applications. In contrast, biomass and agricultural waste-based adsorbents, such as biochar from rice straw or Juglans regia shells, have a much lower cost with varying capacities depending on the type of modification. *H. illucens* LS from this study displayed adsorption performance comparable to other adsorbents (9.80–17.03 mg/g) but with the lowest production cost, making it a very economical and potential option for large-scale water treatment, especially in low-income areas.

CONCLUSIONS

This study demonstrates that *H. illucens* LS can function as an effective and selective unactivated biosorbent for mixed heavy metal wastewater. The heterogeneous protein–chitin–melanin matrix provides diverse functional groups that govern adsorption selectivity, resulting in a preferential uptake order of Fe(III) > Pb(II) >> Cu(II), driven primarily by charge density and competitive surface complexation rather than surface area. Kinetic, isotherm, and thermodynamic analyses indicate a hybrid adsorption mechanism involving rapid physical uptake followed by stronger surface coordination, particularly for Fe(III) and Pb(II). It should be noted that the experiments were conducted under near-neutral pH without active control, where metal immobilization may involve coupled adsorption-hydrolysis processes at the biosorbent interface. Future studies should therefore evaluate pH effects, regeneration, and continuous-flow performance. Overall, *H. illucens* LS represents a low-cost, green, and practically viable biosorbent that enables sustainable valorization of insect-farming waste for multimetal wastewater treatment.

Acknowledgements

The authors gratefully acknowledge the financial support provided by the Ministry of Higher Education, Science, and Technology of the Republic of Indonesia through the 2025 PMDSU Research Grant Scheme, under contract number 109/C3/DT.05.00/PL/2025 dated June 04, 2025, for supporting the main research activities. The authors also wish to thank the Postgraduate Program of Universitas Sriwijaya for providing laboratory facilities during the course of this research.

REFERENCES

1. Alfarra, A., Frackowiak, E., Béguin, F. (2004). The HSAB concept as a means to interpret the adsorption of metal ions onto activated carbons. *Applied Surface Science*, *228*(1–4), 84–92. https://doi.org/10.1016/j.apsusc.2003.12.033
2. Ali, H., Khan, E., Ilahi, I. (2019). Environmental chemistry and ecotoxicology of hazardous heavy metals: Environmental persistence, toxicity, and bioaccumulation. *Journal of Chemistry*, *2019*, 1–14. https://doi.org/10.1155/2019/6730305
3. An, W., Liu, Y., Chen, H., Wang, Q., Hu, X., Di, J. (2024). Oyster shell-modified lignite composite in globular shape as a low-cost adsorbent for the removal of Pb^{2+} and Cd^{2+} from AMD: Evaluation of adsorption properties and exploration of potential mechanisms. *Arabian Journal of Chemistry*, *17*(5), 105732. https://doi.org/10.1016/j.arabjc.2024.105732
4. Azmi, L. S., Jabit, N. 'Ain, Ismail, S., Ku Ishak, K. E. H., Abdullah, T. K. (2025). Membrane filtration technologies for sustainable industrial wastewater treatment: a review of heavy metal removal. *Desalination and Water Treatment*, *323*, 101321. https://doi.org/10.1016/j.dwt.2025.101321
5. Bazan-Wozniak, A., Kovačević, D., Nosal-Wiercińska, A., Pietrzak, R. (2025). Adsorption of ethyl-4-hydroxybenzoate and poly(sodium 4-styrenesulfonate) on activated carbons from *Hermetia illucens* pupal casings: characterization and regeneration. *Measurement*, *252*, 117367. https://doi.org/10.1016/j.measurement.2025.117367
6. Bazan-Wozniak, A., Nosal-Wiercińska, A., Yilmaz, S., Pietrzak, R. (2025). Ethylparaben removal using chitin carbons derived from Hermetia illucens pupa casings. *Diamond and Related Materials*, *158*, 112713. https://doi.org/10.1016/j.diamond.2025.112713
7. Bowron, D. T., Amboage, M., Boada, R., Freeman, A., Hayama, S., Díaz-Moreno, S. (2013). The hydration structure of Cu^{2+}: more tetrahedral than octahedral? *RSC Advances*, *3*(39), 17803. https://doi.org/10.1039/c3ra42400f
8. Dehghani, M. H., Afsari Sardari, S., Afsharnia, M., Qasemi, M., Shams, M. (2023). Removal of toxic lead from aqueous solution using a low-cost adsorbent. *Scientific Reports*, *13*(1), 3278. https://doi.org/10.1038/s41598-023-29674-x
9. Elewa, A. M., Amer, A. A., Attallah, M. F., Gad, H. A., Al-Ahmed, Z. A. M., Ahmed, I. A. (2023). Chemically activated carbon based on biomass for adsorption of Fe(III) and Mn(II) ions from aqueous solution. *Materials*, *16*(3), 1251. https://doi.org/10.3390/ma16031251
10. Fan, C., Wang, B., Feng, H., Zhou, H., Zhang, Y., Ding, W., Liu, F. (2025). Immobilization and coordination chemistry of Friedel's salt (Ca/Al-LDHs) on heavy metals removal. *Process Safety and Environmental Protection*, *193*, 262–271. https://doi.org/10.1016/j.psep.2024.11.035
11. Han, R., Gao, Y., Jia, Y., Wang, S. (2024). Heterogeneous precipitation behavior and mechanism during the adsorption of cationic heavy metals by biochar: Roles of inorganic components. *Journal of Hazardous Materials*, *480*, 136322. https://doi.org/10.1016/j.jhazmat.2024.136322
12. Hidayah, E. N., Mohammad Alghaf Dienullah, R., Maulidifa, N. A., Setiawan, W. (2025). Kinetic adsorption of Fe metal in aqueous solution using maggot shell. *IOP Conference Series: Earth and Environmental Science*, *1454*(1), 012032. https://doi.org/10.1088/1755-1315/1454/1/012032
13. Hussain, M., Ali, V., Pourebrahimi, S., Ahmadi, S., Ghosh, S. (2023). *Chemical Methods of Heavy Metal Management: Coagulation, Flocculation, and Floatation* (pp. 297–312). https://doi.org/10.1021/bk-2023-1456.ch015
14. Imron, M. F., Setiawan, W., Putranto, T. W. C., Abdullah, S. R. S., Kurniawan, S. B. (2024). Biosorption of chromium by live and dead cells of Bacillus nitratireducens isolated from textile effluent. *Chemosphere*, *359*, 142389. https://doi.org/10.1016/j.chemosphere.2024.142389
15. Khayrova, A., Lopatin, S., Varlamov, V. (2021). Obtaining chitin, chitosan and their melanin complexes from insects. *International Journal of Biological Macromolecules*, *167*, 1319–1328. https://doi.org/10.1016/j.ijbiomac.2020.11.086
16. Kothavale, V. P., Sharma, A., Dhavale, R. P., Chavan, V. D., Shingte, S. R., Selyshchev, O., Dongale, T. D., Park, H. H., Zahn, D. R. T., Salvan, G., Patil, P. B. (2023). Carboxyl and thiol-functionalized magnetic nanoadsorbents for efficient and simultaneous removal of Pb(II), Cd(II), and Ni(II) heavy metal ions from aqueous solutions: Studies of adsorption, kinetics, and isotherms. *Journal of Physics and Chemistry of Solids*, *172*, 111089. https://doi.org/10.1016/j.jpcs.2022.111089
17. Kumar, P. S., Korving, L., van Loosdrecht, M. C. M., Witkamp, G.-J. (2019). Adsorption as a technology to achieve ultra-low concentrations of phosphate: Research gaps and economic analysis. *Water Research X*, *4*, 100029. https://doi.org/10.1016/j.wroa.2019.100029
18. Li, P., Fu, T., Gao, X., Zhu, W., Han, C., Liu, N., He, S., Luo, Y., Ma, W. (2019). Adsorption and reduction transformation behaviors of Cr(VI) on mesoporous polydopamine/titanium dioxide composite nanospheres. *Journal of Chemical & Engineering Data*, *64*(6), 2686–2696. https://doi.org/10.1021/acs.jced.9b00111

19. Mei, Y., Zhuang, S., Wang, J. (2025). Adsorption of heavy metals by biochar in aqueous solution: A review. *Science of The Total Environment*, *968*, 178898. https://doi.org/10.1016/j.scitotenv.2025.178898
20. Motitswe, M. G., Badmus, K. O., Khotseng, L. (2022). Development of adsorptive materials for selective removal of toxic metals in wastewater: A review. *Catalysts*, *12*(9), 1057. https://doi.org/10.3390/catal12091057
21. Muharja, M., Fadilah, S. N., Arimbawa, I. M., Hasanah, S., Darmayanti, R. F., Rois, M. F., Asrofi, M. (2022). Low-cost, sustainable, and high-capacity magnetite–cellulose adsorbent from Ramie stem (*Boehmeria nivea* L.) as oil spill solution. *Chemical Papers*, *76*(12), 7429–7440. https://doi.org/10.1007/s11696-022-02423-6
22. Muharja, M., Hasanah, S., Sari, D. A. D., Khoirunnafiuddin, M., Fadilah, S. N., Darmayanti, R. F., Satrio, D., Ismayati, M. (2023). Enhanced oil removal by graphene oxide/N,N′-methylene bisacrylamide modified magnetite-cellulose aerogel derived from ramie stem waste: Adsorption performance, kinetics, and economical analysis. *Bioresource Technology Reports*, *24*, 101645. https://doi.org/10.1016/j.biteb.2023.101645
23. Ouyang, E., Wu, M., He, W., Liu, H., Gui, M., Yang, H. (2024). Chitin/calcite composite extracted from shell waste as a low-cost adsorbent for removal of tetracycline and ciprofloxacin: Effects and mechanisms. *Chemosphere*, *353*, 141503. https://doi.org/10.1016/j.chemosphere.2024.141503
24. Panja, E., Alfredy, T., Elisadiki, J., Jande, Y. A. C. (2025). Hermetia illucens pupae casings and biogas slurry activated carbon electrodes for Cd^{2+} removal from aqueous solutions using capacitive deionization. *Desalination and Water Treatment*, *322*, 101118. https://doi.org/10.1016/j.dwt.2025.101118
25. Patel, P. K., Pandey, L. M., Uppaluri, R. V. S. (2024). Highly effective removal of multi-heavy metals from simulated industrial effluent through an adsorption process employing carboxymethyl-chitosan composites. *Environmental Research*, *240*, 117502. https://doi.org/10.1016/j.envres.2023.117502
26. Pedrazzani, C., Righi, L., Vescovi, F., Maistrello, L., Caligiani, A. (2024). Black soldier fly as a New chitin source: Extraction, purification and molecular/structural characterization. *LWT*, *191*, 115618. https://doi.org/10.1016/j.lwt.2023.115618
27. Perwitasari, D. S., Muryanto, S., Jamari, J., Bayuseno, A. P. (2018). Kinetics and morphology analysis of struvite precipitated from aqueous solution under the influence of heavy metals: Cu^{2+}, Pb^{2+}, Zn^{2+}. *Journal of Environmental Chemical Engineering*, *6*(1), 37–43. https://doi.org/10.1016/j.jece.2017.11.052
28. Phasukarratchai, N., Chaleampatthanapong, N., Wongkaew, P., Boonnontae, R., Wongpram, P., Bumrungwaen, T., Pansak, W., Rongsayamanont, W. (2025). Black soldier fly pupal ExuviExperimentae as a biomaterial for cadmium adsorption: Characterization, efficiency and pot. *Water, Air, & Soil Pollution*, *236*(15), 1008. https://doi.org/10.1007/s11270-025-08656-x
29. Phasuphan, W., Praphairaksit, N., Imyim, A. (2019). Removal of ibuprofen, diclofenac, and naproxen from water using chitosan-modified waste tire crumb rubber. *Journal of Molecular Liquids*, *294*, 111554. https://doi.org/10.1016/j.molliq.2019.111554
30. Radovanovic, D., Dikić, J., Štulović, M., Anđić, Z., Kamberović, Ž., Jevtić, S. (2023). Sorption of Pb^{2+}, Zn^{2+}, Cu^{2+} and Ni^{2+} ions on Na-enriched natural zeolite for wastewater treatment process: A kinetic approach. *Metallurgical and Materials Engineering*, *29*(3), 20–35. https://doi.org/10.56801/MME1007
31. Rahmanian, O., Maleki, M. H., Dinari, M. (2017). Ultrasonically assisted solvothermal synthesis of novel Ni/Al layered double hydroxide for capturing of Cd(II) from contaminated water. *Journal of Physics and Chemistry of Solids*, *110*, 195–201. https://doi.org/10.1016/j.jpcs.2017.06.018
32. Rouquerol, J., Avnir, D., Fairbridge, C. W., Everett, D. H., Haynes, J. M., Pernicone, N., Ramsay, J. D. F., Sing, K. S. W., Unger, K. K. (1994). Recommendations for the characterization of porous solids (Technical Report). *Pure and Applied Chemistry*, *66*(8), 1739–1758. https://doi.org/10.1351/pac199466081739
33. Sekaringgalih, R., Ahmad, A., Nizar, M., Rahmawati, I., Palupi, B., Muharja, M., Rizkiana, M. F., Khotimah, H. (2025). *Synthesis of dithizone immobilized chitosan-silica as an adsorbent of Cr ions in electroplating liquid waste*. 21–31. https://doi.org/10.4028/p-tH12Zp
34. Setiawan, W., Fadilah, S. N., Nurhafizah, P., Gulo, F. (2026). Initial application of Cd/Cu layered hydroxide chloride as adsorbent for Congo Red removal from aqueous solution enhanced by ultrasonication. *Journal of Physics and Chemistry of Solids*, *211*, 113448. https://doi.org/10.1016/j.jpcs.2025.113448
35. Sharma, R. D., Thangadurai, P. (2025). Sustainable bioprocessing of *Hermetia illucens* exuviae into structurally defined chitooligosaccharides within a circular biorefinery framework. *Bioresource Technology Reports*, *32*, 102400. https://doi.org/10.1016/j.biteb.2025.102400
36. Sun, T., Pei, P., Sun, Y., Xu, Y., Jia, H. (2022). Performance and mechanism of As(III/V) removal from aqueous solution by novel positively charged animal-derived biochar. *Separation and Purification Technology*, *290*, 120836. https://doi.org/10.1016/j.seppur.2022.120836
37. Sverguzova, S. V., Bomba, I. V., Pendyurin, E. A. (2021). Sorption extraction of Zn^{2+} ions from aqueous

environment with zoo compost of black soldier fly. In: Klyuev, S.V., Klyuev, A.V. (Eds) Proceedings of the International Conference Industrial and Civil Construction 2021. ICICC 2021. Lecture Notes in Civil Engineering, vol. 147. Springer, Cham. https://doi.org/10.1007/978-3-030-68984-1_49

38. Tran, T.-K., Leu, H.-J., Chiu, K.-F., Lin, C.-Y. (2017). Electrochemical treatment of heavy metal-containing wastewater with the removal of COD and heavy metal ions. *Journal of the Chinese Chemical Society*, *64*(5), 493–502. https://doi.org/10.1002/jccs.201600266
39. Van, H. T., Nguyen, L. H., Nguyen, V. D., Nguyen, X. H., Nguyen, T. H., Nguyen, T. V., Vigneswaran, S., Rinklebe, J., Tran, H. N. (2019). Characteristics and mechanisms of cadmium adsorption onto biogenic aragonite shells-derived biosorbent: Batch and column studies. *Journal of Environmental Management*, *241*, 535–548. https://doi.org/10.1016/j.jenvman.2018.09.079
40. Vigdorowitsch, M., Pchelintsev, A., Tsygankova, L., Tanygina, E. (2021). Freundlich isotherm: An adsorption model complete framework. *Applied Sciences*, *11*(17), 8078. https://doi.org/10.3390/app11178078
41. Wang, X., Wang, X., Chen, W., Yuan, J., Zhang, Q. (2025). Adsorption of Cu(II) and Pb(II) in aqueous solution by biochar composites. *ACS Omega*, *10*(14), 13816–13828. https://doi.org/10.1021/acsomega.4c06837
42. Waśko, A., Bulak, P., Polak-Berecka, M., Nowak, K., Polakowski, C., Bieganowski, A. (2016). The first report of the physicochemical structure of chitin isolated from Hermetia illucens. *International Journal of Biological Macromolecules*, *92*, 316–320. https://doi.org/10.1016/j.ijbiomac.2016.07.038
43. Yang, R., Lu, H., Zhou, J., Qi, L., Wu, X., Rezakazemi, M., Ge, S. (2025). Next-generation biomass nanocomposites for heavy metal ion adsorption: innovations and environmental impact. *Separation and Purification Technology*, *370*, 133157. https://doi.org/10.1016/j.seppur.2025.133157
44. Zainudin, N. I., Bin Md.Rashid, R. I., Ishak, A. R., Ali, A. (2023). Removal of lead (Pb) from aqueous solutions using exoskeleton of black solider fly (BSF). *Environment-Behaviour Proceedings Journal*, *8*(25), 175–184. https://doi.org/10.21834/e-bpj.v8i25.4864
45. Zewude, D. A., Noguchi, T., Sato, K., Izawa, H., Ifuku, S. (2022). Production of chitin nanoparticles by bottom-up approach from alkaline chitin solution. *International Journal of Biological Macromolecules*, *210*, 123–127. https://doi.org/10.1016/j.ijbiomac.2022.05.006
46. Zhang, H., Dang, Q., Liu, C., Yu, D., Wang, Y., Pu, X., Liu, Y., Liang, Y., Cha, D. (2019). Fabrication of methyl acrylate and tetraethylenepentamine grafted magnetic chitosan microparticles for capture of Cd(II) from aqueous solutions. *Journal of Hazardous Materials*, *366*, 346–357. https://doi.org/10.1016/j.jhazmat.2018.12.006
47. Zhang, M., Tang, Z., Zhao, Y., Wang, X., Xu, X. (2020). Study on the adsorption properties of different insect feces on Cu^{2+} and Cd^{2+}. *IOP Conference Series: Earth and Environmental Science*, *450*(1), 012124. https://doi.org/10.1088/1755-1315/450/1/012124
48. Zhao, R., Zheng, H., Zhong, Z., Zhao, C., Sun, Y., Huang, Y., Zheng, X. (2021). Efficient removal of diclofenac from surface water by the functionalized multilayer magnetic adsorbent: Kinetics and mechanism. *Science of The Total Environment*, *760*, 144307. https://doi.org/10.1016/j.scitotenv.2020.144307
49. Zhibo, S., Liyi, L., Yong, H., Jie, B. (2018). Influence on ferric chloride aqueous solution caused by external electrostatic field: a molecular dynamics simulation study. *RSC Advances*, *8*(68), 38706–38714. https://doi.org/10.1039/C8RA08349E
50. Złotko, K., Waśko, A., Kamiński, D. M., Budziak-Wieczorek, I., Bulak, P., Bieganowski, A. (2021). Isolation of chitin from black soldier fly (*Hermetia illucens*) and its usage to metal sorption. *Polymers*, *13*(5), 818. https://doi.org/10.3390/polym13050818